ACS OMEGA

http://pubs.acs.org/journal/acsodf

Article

Toward the Separation of Different Heating Mechanisms in Magnetic Particle Hyperthermia

Eirini Myrovali, Kyrillos Papadopoulos, Georgia Charalampous, Paraskevi Kesapidou, George Vourlias, Thomas Kehagias, Makis Angelakeris, and Ulf Wiedwald*

Cite This: *ACS Omega* 2023, 8, 12955−12967

Read Online

ACCESS | Metrics & More | Article Recommendations | Supporting Information

ABSTRACT: Magnetic particle hyperthermia (MPH) is a promising method for cancer treatment using magnetic nanoparticles (MNPs), which are subjected to an alternating magnetic field for local heating to the therapeutic range of 41−45 °C. In this window, the malignant regions (i.e., cancer cells) undergo a severe thermal shock while healthy tissues sustain this thermal regime with significantly milder side effects. Since the heating efficiency is directly associated with nanoparticle size, MNPs should acquire the appropriate size to maximize heating together with minimum toxicity. Herein, we report on facile synthetic controls to synthesize MNPs by an aqueous precipitation method, whereby tuning the pH values of the solution (9.0−13.5) results in a wide range of average MNP diameters from 16 to 76 nm. With respect to their size, the structural and magnetic properties of the MNPs are evaluated by adjusting the most important parameters, i.e. the MNP surrounding medium (water/agarose), the MNP concentration (1−4 mg mL^{-1}), and the field amplitude (20−50 mT) and frequency (103, 375, 765 kHz). Consequently, the maximum heating efficiency is determined for each MNP size and set of parameters, outlining the optimum MNPs for MPH treatment. In this way, we can address the different heat generation mechanisms (Brownian, Néel, and hysteresis losses) to different sizes and separate Brownian and hysteresis losses for optimized sizes by studying the heat generation as a function of the medium viscosity. Finally, MNPs immobilized into agarose solution are studied under low-field MPH treatment to find the optimum conditions for clinical applications.

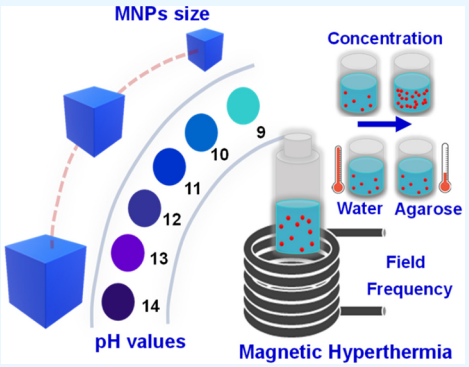

1. INTRODUCTION

Magnetic nanoparticles (MNPs) with typical sizes ranging from 1 to 100 nm have been successfully applied in different applications such as electronics, energy storage, sensing, water purification, hybrid magnetic stents, and therapeutic platforms.[1−6] One of the most promising applications is magnetic particle hyperthermia (MPH), defined as a least-invasive cancer therapy exploiting heat generation (41−45 °C) by MNPs when these are exposed to an alternating magnetic field (80−800 kHz). In the quest of magnetic nanomaterials for MPH, iron oxide is the material of choice thanks to good biocompatibility and the ability of magnetite MNPs to address various theranostic approaches simultaneously (e.g., contrast agents in magnetic resonance imaging, drug-cargo carriers, mechanical actuators, heating agents). Moreover, they follow a well-known metabolic pathway in the human body.[7,8] Specifically, iron oxide MNPs with superparamagnetic behavior (MLF AS, MagForce Nanotechnologies AG, Berlin, Germany, 15 nm) have been approved for clinical trials on patients with glioblastoma multiforme[9−11] or prostate cancer.[12,13]

Various routes for synthesizing iron oxide nanoparticles have been proposed over the past decades, where MNPs can be prepared either by top-down or bottom-up methodologies.[14] The aqueous precipitation method is a bottom-up, cost-effective, fast process and easily expandable to an industrial level.[15,16] Compared to other synthetic routes, the precipitation pathway is generally preferred due to its high yield, facile control, and very-low-cost production.[17] Moreover, the reagents for the preparation of magnetite nanoparticles are nontoxic and eco-friendly. It is the simplest method to prepare MNPs from salt(s), forming Fe^{2+} and Fe^{3+} ions in water. Moreover, fine-tuning of the synthesis (temperature, pH, pressure, and reaction time) allows for controlling size, polydispersity, phase, and surface chemistry of the resultant MNPs.[18−20]

However, one of the challenges using magnetic nanomaterials for MPH is to induce the highest heating efficiency to reduce dosage and subsequent toxicity.[21] There are different ways to improve the heat release: (a) the magnetocrystalline anisotropy of MNPs (b) the MNP size, (c) the dosage and the

Received: January 10, 2023
Accepted: March 3, 2023
Published: March 30, 2023

medium of MNPs, and (d) MPH parameters such as the AC field amplitude and frequency. The heating efficiency strongly correlates with the magnetic features of the MNPs, such as magnetization and coercive field, which in turn depend on size.[22−24] Magnetite nanoparticles exhibit superparamagnetic (SPM) behavior at physiological temperature, for particle diameters of up to 20−25 nm. An increase of the MNP diameter leads to single-domain MNPs with ferromagnetic (FM) behavior up to diameters of ∼70−90 nm, where MNPs turn to multidomain (MD) magnetic configurations.[25] The losses in the SPM regime are attributed to Néel and Brownian loss mechanisms. With increasing average MNP size, the prevailing heating mechanism originates from the hysteresis losses, suggesting that the heat in the FM MNPs is produced by their hysteresis loops.[26,27] Thus, with respect to their size, MNPs produce heat due to different mechanisms.

Another approach to further optimize the heating efficiency may be achieved by tuning the MNP−medium parameters such as dosage (namely MNP concentration) and the viscosity of the medium based on a water/agarose solution. In clinical practice, the iron concentration typically varies between 0.5 and 8.0 mg mL^{-1} in *in vitro* studies.[28,29] At higher concentration, the shorter the interparticle distance between MNPs, the greater their dipolar interaction with a direct impact on eventual heat release.[30,31] Further, recent studies have shown that the heating efficiency changes as a function of the viscosity of the medium.[32−35] However, there have been only a few studies addressing the different heating mechanisms as a function of medium viscosity.[36,37] Finally, for a given set of particle size, magnetic anisotropy, dipolar interactions, and the medium, the external field amplitude and frequency should match the MNP features for the largest heat release in MPH. Using an optimized set of parameters, heat release can be tuned by adjusting the field amplitude or frequency. In most studies, the range of the frequencies and AC fields are between 80 and 800 kHz and betweem 1 and 60 mT, respectively.[38−41]

Considering the interplay of all these parameters, we study here magnetite MNPs in a wide size range for improvement and optimization of the heating efficiency. The medium and the field are varied to cover the wide parameter range of MPH. First, magnetite MNPs with diameters of 16−76 nm are synthesized by chemical precipitation (SPM to FM size range) by tuning the pH value from 9 to 13.5 (Scheme 1a). The crystal structure, average size, and morphology were evaluated by X-ray diffraction (XRD), transmission electron microscopy (TEM), and high-resolution TEM (HRTEM), while the collective magnetic features were recorded by DC magnetometry. Eventually, magnetic particle hyperthermia was conducted by adjusting medium parameters, concentration (1−4 mg mL^{-1}), type (water/agarose), or the AC field amplitude (20−50 mT) and frequency (103, 375, 765 kHz), as shown in Scheme 1b. Accordingly, with respect to the MNP size, the heating efficiency is determined and optimized for certain sets of parameters, outlining the feasibility of size dependences on heat generation. The particle size and concentration play an important role to control the heat rate in the MPH, while the viscosity of the medium affects the heating mechanisms. The highlight of the current work is the determination and evaluation of the heating efficiency optimum conditions for further biomedical applicability. Although in water the specific loss power is substantially larger when compared to high concentrations of phantoms of agarose mimicking tissues, we successfully circumvent this by disentangling relaxation and hysteresis losses in by particle (size) and field (amplitude/frequency), holding the biomedical constraint field-frequency criterion ($Hf \leq 10^9$ A m^{-1} s^{-1}).

Scheme 1. (a) Generation of Magnetite MNPs by Chemical Coprecipitation for Differently Sized MNPs from 16 to 76 nm by Choosing the pH Value from 9.0 to 13.5 during Synthesis and (b) MPH Conducted by Adjusting Medium Parameters: Concentration (1−4 mg mL^{-1}), Type (Water/Agarose), or AC Field Amplitude (20-50 mT) and Frequency (103, 375, 765 kHz)

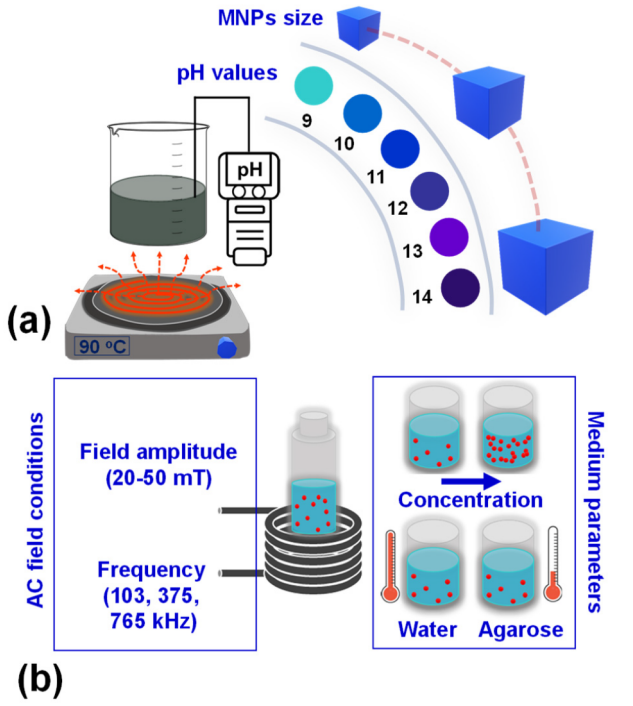

2. EXPERIMENTAL SECTION

2.1. Synthesis of MNPs. Magnetite nanoparticles were synthesized by an oxidative aqueous precipitation method of iron salts following a typical route described in detail in a previous study.[42] The size of MNPs was controlled through the nature of sodium hydroxide (NaOH). First, a solution of sodium nitrate ($NaNO_3$; 0.2 M) was mixed with ethanol and water (1:1 ratio). This initial solution we call solution A in the following. Second, a mixture of iron(II) sulfate heptahydrate ($FeSO_4{\cdot}7H_2O$; 0.2 M) and sulfuric acid (H_2SO_4; 0.01 M) were added to solution A and rigorously stirred. During the mixture, NaOH (0.4 M) solution was added drop by drop to stabilize the chosen pH value (pH 9.0−13.5, Table 1). The final solution was heated to 90 °C for 3 h. Subsequently, the solution was cooled to room temperature. Finally, the solid was separated by magnetic decantation and washed several times with distilled water.

MNPs were dispersed into agarose gel to examine the heating mechanisms during MPH. Agarose gel thereby prevents movement of MNPs during the experiment. In a typical procedure, 4 mg of MNPs and agarose content (varying from 2.5 to 30 mg) were added to 1 mL of deionized water. Then, the solution was sonicated for 3 min. Afterward, the solution was placed in a water bath at 84 °C for 10 min under continuous stirring. Finally, the agarose gel was obtained by rapid cooling the liquid in an ice bath.

https://doi.org/10.1021/acsomega.2c05962
ACS Omega 2023, 8, 12955−12967

Table 1. Overview of Morphological and Magnetic Features of MNPs for Variable pH Values of the Synthesis. All data refer to 300 K.

pH	d_{TEM} (nm)[a]	d_{XRD} (nm)[b]	$\mu_o H_C$ (mT)	M_s (A m^2 kg^{-1})	M_r (A m^2 kg^{-1})	M_r/M_s
13.5	76 ± 35	71 ± 16	5.2	85	3.6	0.042
12.0	37 ± 20	34 ± 14	7.4	81	6.2	0.077
11.0	34 ± 15	31 ± 12	8.4	77	7.7	0.100
10.0	20 ± 12	19 ± 10	7.4	76	7.5	0.098
9.0	16 ± 10	14 ± 10	1	59	0.7	0.011

[a]As derived from TEM. [b]As derived from XRD using Scherrer's formula.

2.2. Characterization of MNPs. The crystal structure of the MNPs was identified by X-ray diffraction (XRD) using a two-cycle Rigaku Ultima+ X-ray diffractometer with Cu K_α radiation operating at 40 kV and 30 mA. The increment of angle 2θ was kept constant at 0.05°, while data acquisition dwell time was set at 3 s in Bragg–Brentano geometry. To investigate the morphology, size, and microstructure of the MNPs and their distributions, samples for transmission electron microscopy (TEM) were prepared by drop-casting the colloidal dispersions onto carbon-coated Cu grids after sonication for 1 h in water. TEM and high-resolution TEM (HRTEM) were performed with a JEOL 2011 UHR microscope with a 0.194 nm point resolution operated at 200 kV. Magnetic hysteresis loops (major loops at ±3 T and minor loops from ±20 to ±50 mT corresponding to the AC magnetic field in MPH) were recorded at 300 K by vibrating sample magnetometry (VSM) in a Quantum Design Dynacool PPMS system.

2.3. Magnetic Hyperthermia. Three different induction heating setup systems were used for magnetic heating operating at 765 kHz (SPG-10 Ultrahigh Frequency Induction Heating Machine, Shuangping Corporation) and 375 kHz (2.4 kW Easyheat/Ambrell), respectively. Hyperthermia experiments at low frequency (103.6 kHz) were performed using a MagneTherm device (Nanotherics). The amplitude of the magnetic field varied from 20 to 50 mT. The temperature was recorded by using a GaAs-based optical fiber probe. Each measurement cycle included a heating and a cooling stage. The heating efficiency is quantified by the specific loss power (SLP) determined as the power absorption per unit mass of magnetic material (in W g^{-1}) following a standardized procedure as described in a previous work[43] to provide reliable, reproducible SLP values solely of magnetic origin using the equation

$$\mathrm{SLP} = C\frac{\Delta T}{\Delta t}\frac{m_f}{m_{MNPs}} \quad (1)$$

where C is the volumetric specific heat capacity of the sample, m_f is the mass of the dispersion, m_{MNPs} is the magnetic nanoparticle (magnetite) mass in the colloidal dispersion, and $\Delta T/\Delta t$ is the average value of the maximum slope at the initial stage of heating after switching on the AC magnetic field. The heating rate was determined from heating curves after the adiabatic corrections.[43]

3. RESULTS AND DISCUSSION

3.1. Structure and Magnetism of MNPs. The structure of the MNPs was determined by XRD, as shown in Figure 1. All samples have the inverse spinel structure of iron oxides, with strong similarities among them, as clearly outlined by the presence of magnetite peaks with the major one corresponding to the (311) reflection of bulk magnetite. Additional characteristic reflections of magnetite at (220), (222), (400), (422), (440), (511), and (440) are also present (PDF #75-0033). Narrow and well-defined diffraction peaks are indicative of the high level of crystallinity of MNPs. It was found that the crystallite size of MNPs varied from 14 to 71 nm as shown in Table 1 by implementing the Scherrer equation (2)

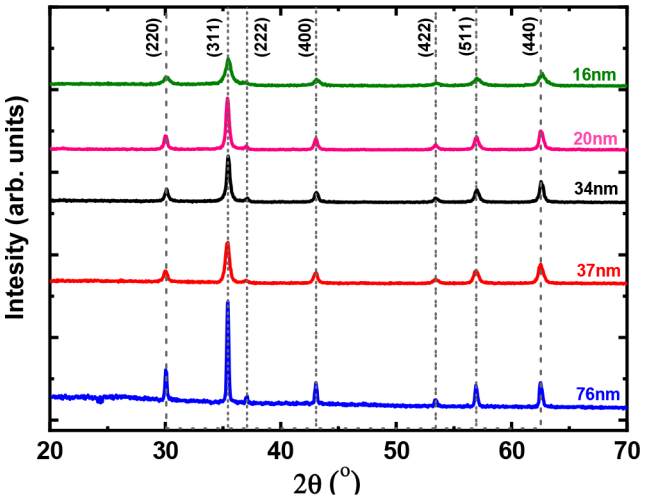

Figure 1. XRD of magnetite MNPs with varying particle sizes of 16 to 76 nm using Cu K_α radiation.

$$d_{XRD} = \frac{0.9}{\beta}\frac{\lambda}{\cos\theta} \quad (2)$$

where λ is the wavelength of X-rays, β is the width (full width at half-maximum) of the X-ray diffraction peak in radians, and θ is the Bragg angle.

TEM and HRTEM imaging and selected area electron diffraction (SAED) analysis were utilized for the morphological and structural characterization of the MNPs at the nanoscale (Figure 2). As shown in the TEM images of Figures 2a–e, MNPs that were prepared using different pH values exhibit a wide range of sizes (16–76 nm) and shapes (cuboids to spheroids). The size distributions of the MNPs are collected in Figure S1. TEM observations reveal that the size of the MNPs increases with increasing pH value. This phenomenon is due to larger quantities of OH^- included in the double-layered hydroxide structure of the green rust.[44,45] The mixture of ferrous and ferric iron hydroxides based on the brucite $Fe(OH)_2$ layers is referred as green rust, where part of Fe^{2+} is oxidized to Fe^{3+} and anions and water molecules are in the interlaminar space.[46] Thus, on increasing the OH^- (high pH values), the MNPs are grown by slow diffusion of $Fe(OH)_2$ species to the primary particles as a result of larger magnetite particles.

https://doi.org/10.1021/acsomega.2c05962
ACS Omega 2023, 8, 12955−12967

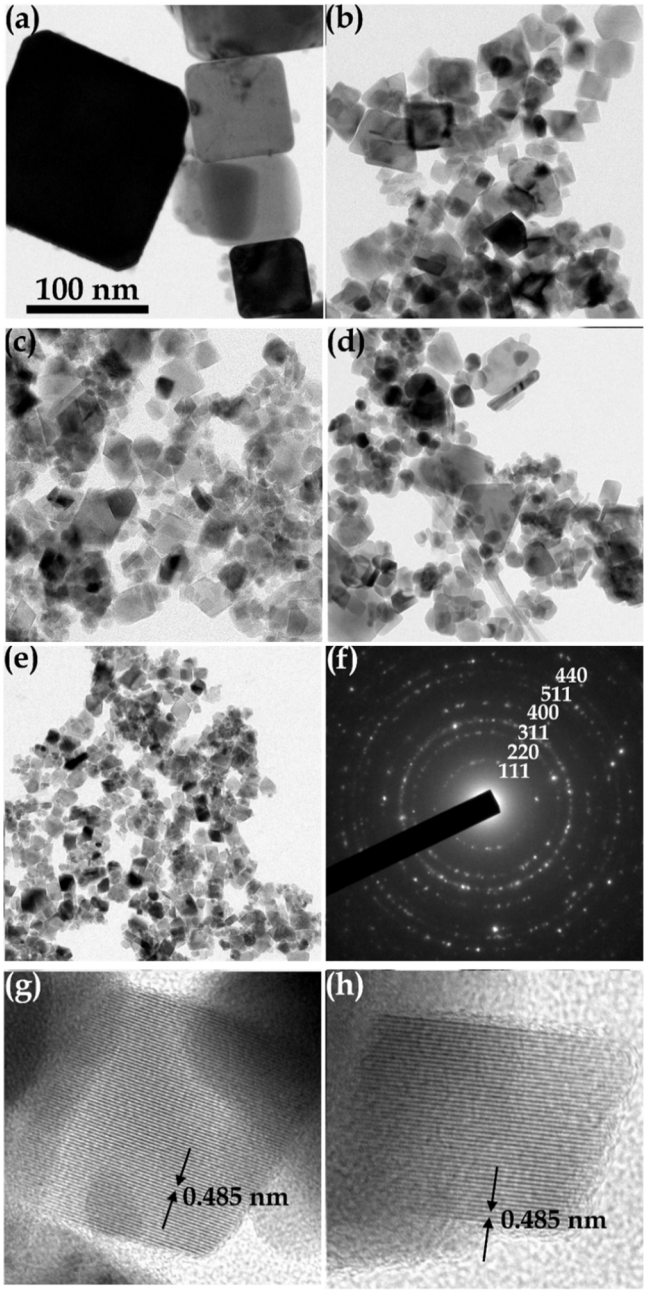

Figure 2. (a−e) TEM images of the MNPs, prepared at pH values of 13.5, 12.0, 11.0, 10.0, and 9.0, respectively, showing their morphology and sizes on an identical scale. (f) Typical SAED ring pattern from the sample prepared at pH 9, corresponding to all cases, where the reflections of the main crystal planes of the magnetite lattice are denoted. (g, h) HRTEM images of individual MNPs, from the samples prepared at pH values of 12.0 and 11.0, respectively, illustrating the high crystallinity of the MNPs, where the interplanar spacings of the (111) planes (0.485 nm) of magnetite are clearly resolved.

In contrast, with a decrease in the OH^- (low pH values), the MNPs grow much faster, creating small particles. Moreover, the shapes of the MNPs are, generally, cuboctahedra for pH values >11 (Figure 2a,b), while lower pH values (pH ≤ 11) lead to faceted shapes of the MNPs (Figures 2c−e). Faster growth of [100] or [110] crystallographic directions, due to lower surface energies over the [111] direction, lead to cuboctahedra or faceted shapes, respectively.[47,48]

In Figure 2f, a typical SAED pattern common for all cases of the MNPs is shown, exhibiting spotty diffraction rings that imply the single-crystalline nature of randomly oriented MNPs. The *d* spacing values of the crystal planes measured from the SAED rings in reciprocal space, namely the (111), (220), (331), (400), (422), (511), and (440) planes, correspond to the cubic spinel structure of the magnetite phase. Moreover, HRTEM imaging of individual MNPs (Figures 2g,h), regardless of the pH value, confirmed that the *d* spacing values measured in real space from the MNPs belong indeed to the magnetite phase, while the single-crystalline nature of the MNPs is evident. The small difference between particle size and crystallite size (Table 1) confirms the single-crystalline nature of the samples.

Figure 3a shows hysteresis loops for 16−76 nm MNPs at room temperature (300 K) under an externally applied

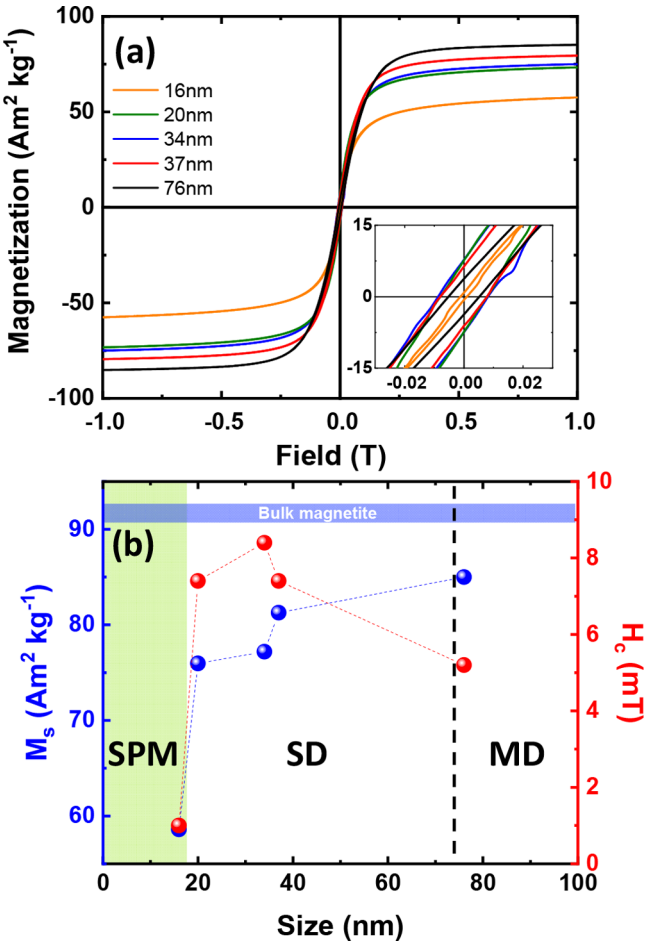

Figure 3. (a) Hysteresis loops for 16−76 nm MNPs measured under ±1 T. The insets show a magnification around zero field. (b) Size dependence of saturation magnetization (blue spheres) and coercive field (red spheres). The expected ranges of the superparamagnetic (SPM), single-domain (SD), and multidomain (MD) regions are indicated.

magnetic field of ±1 T. It important to know that the saturation magnetization and coercive field increase with the particle size.[20] The bulk value of saturation magnetization of magnetite at room temperature is 92 A m^2 kg^{-1}, as shown by the shaded band in Figure 3b.[49] Starting from small MNPs with an average diameter of 16 nm, the saturation magnet-

https://doi.org/10.1021/acsomega.2c05962
ACS Omega 2023, 8, 12955−12967

ization was 59 A m^2 kg^{-1} and the remanence magnetization and the coercive field were almost zero (Table 1).

Overall, we obtain a reduction of the saturation magnetization as compared to the bulk value of magnetite. This phenomenon could arise from the bare surface resulting from the reduced number of nearest-neighbor oxygen atoms surrounding the octahedral iron, which is 5 instead of 6 as in bulk magnetite.[50] Another reason for this reduction of saturation magnetization could be ascribed to surface spin disorder or collective oscillation.[51] Such a reduction of the saturation magnetization is in good agreement with the previous works presenting size-dependent magnetization data.[52,53] For MNPs with sizes of 20−76 nm, the saturation magnetization increases from 76 to 85 A m^2 kg^{-1}, as shown in Figure 3b. Nonetheless, we obtain M_s values close to those of bulk magnetite. Concerning the remanent magnetization, the obtained squareness M_r/M_s values (Table 1) are very small ($M_r/M_s \leq 0.1$), much smaller than those expected for noninteracting randomly oriented nanoparticles with uniaxial M_r/M_s (~0.5) or cubic magnetic anisotropy ($M_r/M_s \approx 0.83$) at low temperatures, according to the Stoner−Wohlfarth model. This reduction in the remanence of the nanoparticles can be attributed to the effect of the dipolar interactions between the nanoparticles.[54−56] The coercive field is almost constant (7.4 to 8.4 mT for MNPs with sizes of 20 and 34 nm, respectively), as shown in Figure 3b. Beyond the maximum coercive field value, there is a reduction from 8.4 to 5.2 mT for MNPs with sizes of 34 and 76 nm, respectively. The reduction in the coercive field values is close to the reported value (10−5 mT), considering that the magnetization reversal takes place by a coherent mechanism following the Stoner−Wohlfarth model.[49] These results confirm that the small MNPs (16 nm) exhibit typical SPM behavior, while when the size is increased (>16 nm) the MNPs are in a ferromagnetic state (single-domain (SD) region). The same behavior as a function of size from SPM to ferromagnetic behavior is in good agreement with a previous work.[57] For the largest MNPs of a median size of 76 nm, the size distribution is broad, as shown in Figure S1a, and it presents a large standard deviation, as indicated in Table 1. Considering that their volume is large as compared to the smaller sizes in this sample, the magnetic hysteresis loop is dominated by the large particles and thus shows, effectively, a decreasing coercive field.[58,59] Thus, the larger particles (76 nm) are expected to be in a multidomain (MD) state.

3.2. Magnetic Particle Hyperthermia: Effect of Concentration. The proposed MNP dosage is crucial for an MPH treatment not only for the ultimate heating efficiency but also for side effects and toxicity.[60] A MNP solution may be implemented in clinical protocols, provided it successfully achieves the hyperthermia window of 41−45 °C. To examine indicative dosage schemes, three different concentrations (4, 2, and 1 mg mL^{-1}) were examined for hyperthermia conditions 765 kHz/30 mT. As can be seen in Figure S2a−c, all samples successfully enter in the hyperthermia window at a higher concentration (4 mg mL^{-1}), but when the concentration decreases, samples with sizes of 76 nm (1, 2 mg mL^{-1}) and 16 nm (1 mg mL^{-1}) cannot overcome this limit. The results for the heating rate as a function of MNP concentration are presented in Figure 4a. Higher heating rates directly correspond to more efficient heating. When the heating rate is below 0.06 °C s^{-1} (yellow window in Figure 4a), the samples cannot reach the hyperthermia window. As can be seen, the heating rate increases when the concentration increases from 1

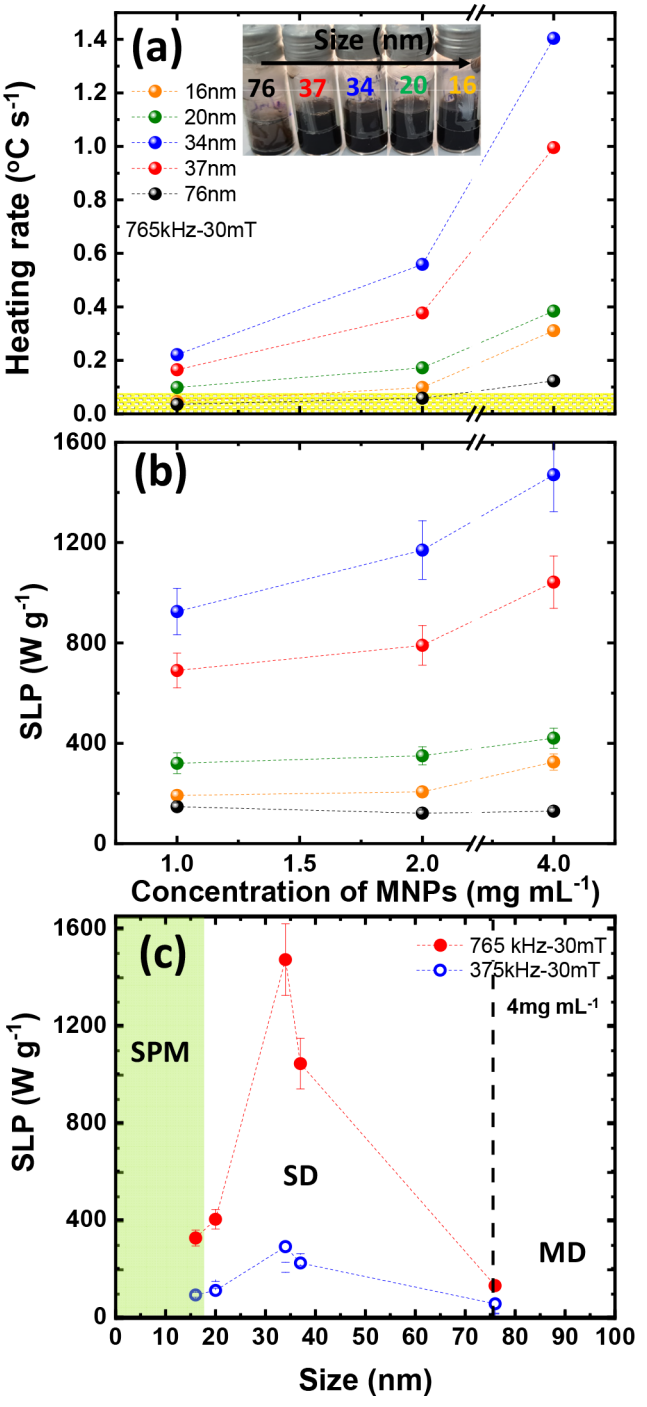

Figure 4. (a) Heating rate as a function of the MNP concentration (765 kHz/30 mT). (b) SLP values against MNP sizes for varying concentrations (1−4 mg mL^{-1}). (c) SLP values as a function of MNP sizes at two different frequencies, 375 kHz (blue color) and 765 kHz (red color). The MNP concentration was kept constant at 4 mg mL^{-1}. Lines are guides to the eye.

to 4 mg mL^{-1} for all samples. The highest heating rates appear in MNPs with sizes of 34 and 37 nm, as shown in Figure 4a in blue and red, respectively.

However, increasing the size further to 76 nm leads to strongly reduced heating rates. Considering that the MNPs are in the MD size regime, as discussed above, the heating rate decreases, since the MNPs reverse magnetization by domain wall motion.[61,62] Another factor that reduces the heating rate is

https://doi.org/10.1021/acsomega.2c05962
ACS Omega 2023, 8, 12955−12967

the colloidal stability in water solution due to the large volume of MNPs. Before the hyperthermia measurements, the large MNPs were precipitating to the bottom of the vial while the other samples formed stable aqueous suspensions (Figure 4a inset). This means that the heating rates would be different at the bottom and the center of the vial. Indeed, a previous work has shown that the time needed to reach the hyperthermia limit on the bottom is 8 times faster than that of the top of the vial.[63]

In all cases, SLP values derived as a function of size were calculated following eq 1 for different MNP concentrations. Note that SLP values are directly proportional to the heating rate ($\Delta T/\Delta t$). The SLP values increase with increasing concentration of MNPs from 1 to 4 mg mL^{-1} in all cases apart from large MNPs (76 nm), as shown in Figure 4b. For large MNPs, no change was detected, which is likely due to a decreased colloidal stability of MNPs, as discussed above. MNPs between 16 and 37 nm are more isolated from each other at low concentrations, since the interparticle dipolar interaction decreases quickly with distance d (proportional to d^{-3}), and SLP values decrease.[64] In contrast, when the concentration of MNPs increases, the interparticle distance decreases and thereby the dipolar interactions increase in the ferrofluid.[65,66] This behavior is confirmed by the increase of the heating efficiency from lower (1 mg mL^{-1}) to higher concentration (4 mg mL^{-1}). On examining the heating rate for different sizes, the slope $\Delta T/\Delta t$ strongly depends on MNP size (Figure 4a). Focusing on the higher concentration of 4 mg mL^{-1}, it was observed that the SLP values increase with size from 16 to 34 nm, while further increase in dimensions causes a reduction in the SLP values (Figure 4c, red symbols). This means that dipolar coupling becomes more important, in line with the increasing magnetic stray field strength per particle.[67]

However, the highest SLP values were obtained for 34 and 37 nm with values of 1450 and 1050 W g^{-1}, respectively, under an AC field of 765 kHz/30 mT. Such behavior may be attributed to the influence of the dipolar interaction in water solutions.[68] When the MNPs are stabilized into agarose gel, the release of the heat varies dramatically with respect to their size. Changing the viscosity of the medium affects the different heating mechanisms of MNPs as a function of size. The same tendency (but less pronounced) of the SLP values as a function of size was also obtained at the lower frequency of 375 kHz (Figure 4c, blue symbols). However, there is a clear reduction of the SLP values with decreasing frequency. This behavior is in good agreement with previous works which have shown that the heating efficiency scales linearly with the frequency.[34,69−71]

For clinical applications, the challenge is to achieve the hyperthermia limit of 41−45 °C using a product field amplitude × frequency lower than 5 × 10^9 A m^{-1} s^{-1}.[72,73] For 765 kHz/30 mT, this product is much higher than this limit. Considering the value of 103 kHz used e.g. for medical treatment, experiments were focused on the samples with higher heating rate/shorter time to reach the hyperthermia limit in order to improve their heating under low-field conditions. From now on, we focus on the samples with sizes ranging from 16 to 37 nm with the higher heating rate and concentration of 4 mg mL^{-1}. The larger MNPs (76 nm) were not further investigated due to their lower heating rate.

3.3. Magnetic Particle Hyperthermia: Effect of the Field Amplitude. The magnetic losses strongly depend on the properties of MNPs and may be determined experimentally by measuring hysteresis loops.[74] The minor loop area is presented in Figure 5a−d from the smallest MNPs (16 nm) to the 37 nm sample. In all cases, the area of hysteresis loops increases with increasing DC applied field from 20 to 50 mT. Small MNPs (16 nm) have extremely narrow loops and low squareness due to the SPM behavior as described above. By increasing the size from 20 to 34 nm, the minor loop areas become wider as compared to the smallest ones. However, as the size of MNPs increases (>34 nm), the area of the minor loops and the magnetization decrease. Thus, the hysteresis loops change as a function of both the size and the applied magnetic field. Thus, it is very crucial to be able to evaluate the hysteresis losses as a function of the applied field and the size of MNPs.

First, the hysteresis loop area of each sample during one cycle of the magnetic field was calculated according to eq 3[75]

$$A = \int_{-H_{min}}^{+H_{max}} \mu_o \mathrm{M(H)}\, \mathrm{d}H \tag{3}$$

where $M(H)$ is the field-dependent MNPs magnetization and $\mu_o H_{max}$ is the amplitude of the magnetic field. The hysteresis losses were estimated using the eq 4[71]

$$\text{hysteresis losses} = Af \tag{4}$$

where area A is the energy loss per cycle and f is the frequency. The area of DC magnetic measurements could be used to estimate the maximum available energy (A) generated every time the field reverses.[76−78] Hysteresis losses (in W g^{-1}) were determined from minor loops after multiplying loop surfaces by the corresponding frequency. Thus, the hysteresis losses calculated using the minor loops proved to be a good indicator to qualitatively compare the heating efficiency of different nanoparticle systems.[79] Figure 6a (open symbols) shows the results of the hysteresis losses using a frequency of 375 kHz. Starting from MNPs with a size of 16 nm, the values from hysteresis losses were too low (up to ∼90 W g^{-1}) because the area of the minor loops becomes extremely small due to SPM behavior. On the other hand, the hysteresis losses for MNP sizes of 20, 34, and 37 nm vary from 50 to 175 W g^{-1}, 85 to 300 W g^{-1} ,and 75 to 240 W g^{-1} with an applied field amplitude of 20−50 mT, respectively. For a better understanding of the differences in heating efficiency as a function of the applied field, hyperthermia measurements were taken as a function of the external field (20−50 mT) using a frequency of 375 kHz while the MNP concentration was kept constant at 4 mg mL^{-1}. The complete set of heating curves in 20−50 mT are presented in Figure S3. Different values are observed on comparing the results between hyperthermia and hysteresis loss measurements, as shown in Figure 6a (closed and open symbols). This means that there are different heat mechanisms as a function of size. However, DC hysteresis losses have the same tendency as AC hyperthermia measurements.

The field-amplitude-dependent SLP appeared to be linear at the lower frequency of 150 kHz, while at higher frequencies (over 300 kHz) there is a deviation from the linear response.[80] Thus, the SLP values follow the expected square dependence with respect to the external field.[22] More specifically, the dependence of the SLP values as a function of the applied field can be described by following eqs 5 and 6[81,82] where the factor a, the coefficient between SLP and H^2, is derived

$$\mathrm{SLP} = aH^2 \tag{5}$$

https://doi.org/10.1021/acsomega.2c05962
ACS Omega 2023, 8, 12955−12967

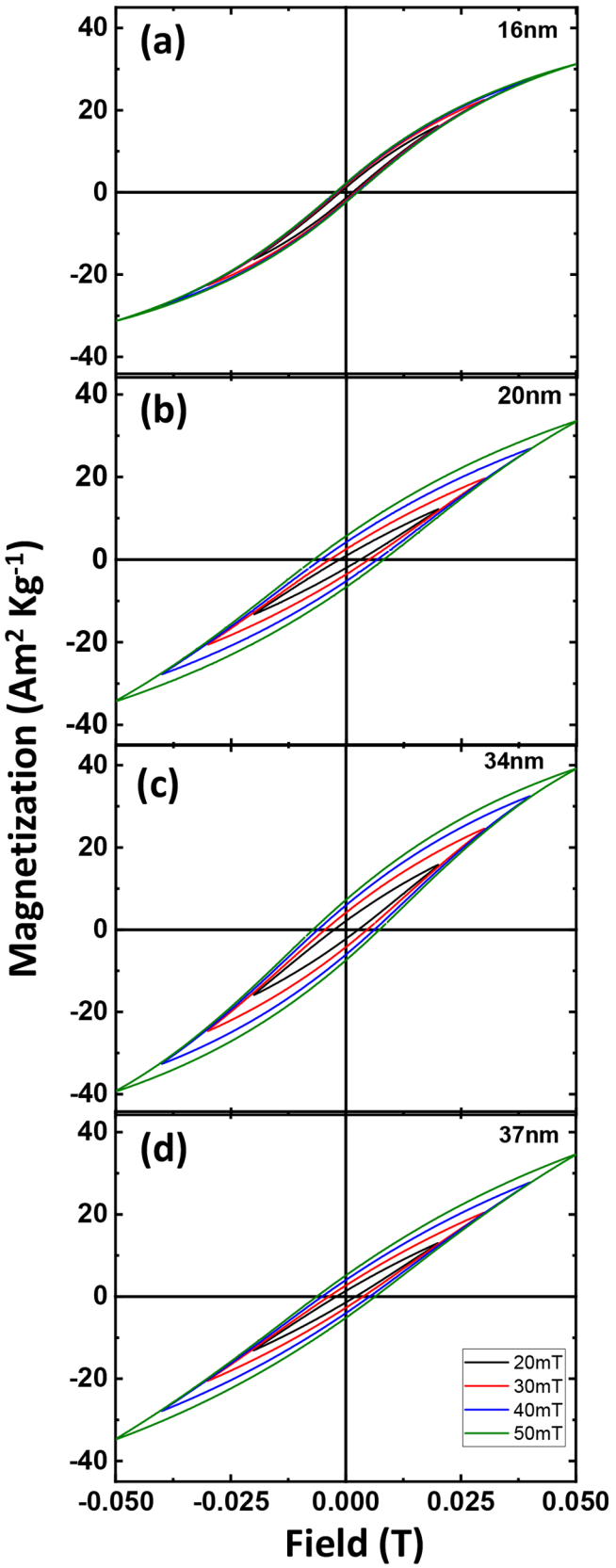

Figure 5. Minor magnetic hysteresis loops as a function of the applied DC field from 20 to 50 mT at room temperature for MNP sizes of (a) 16 nm, (b) 20 nm, (c) 34 nm, and (d) 37 nm.

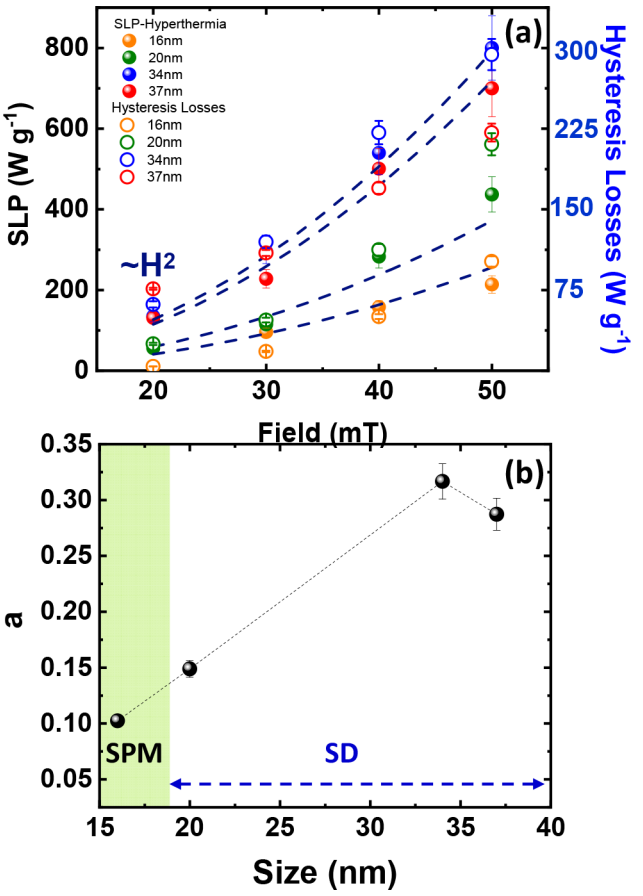

Figure 6. (a) SLP values and DC-hysteresis losses scaled to 375 kHz as a function of field for different MNP sizes from 16 to 37 nm. The concentration was 4 mg mL^{-1}. (b) Fitted factor a as a function of particle size. The line is a guide to the eye.

$$a = \begin{cases} \dfrac{2\pi^2 M_s^2 V \tau_N f^2}{3k_B T \rho} & \text{for } r \leq 19 \text{ nm} \\ \dfrac{M_s^2}{18\eta\rho} & \text{for } r > 19 \text{ nm} \end{cases} \quad (6)$$

where H is the magnetic field, M_s is the saturation magnetization, V is the volume of MNPs, τ_N is the Néel relaxation time, f is the frequency, k_B is Boltzmann's constant, ρ is the density of MNPs, T is the temperature, η is the medium viscosity, and r is the radius of MNPs.

Figure 6b shows the effect of factor a as a function of particle size fitting eq 5. The factor depends on the size and the magnetic profile of the MNPs.[83,84] More specifically, the a factor increases from the SPM to the SD region as shown in Figure 6b. One possible explanation for this behavior is that the SLP value is independent of the medium for small MNPs according to the eq 6. Thus, the main heating mechanism in the SPM region is the Néel relaxation due to internal friction between the crystal lattice and the rotating magnetic spins. In contrast, the medium of MNPs affects only the larger MNPs (>19 nm) according to eq 6. More specifically, the SLP value is inversely proportional to the liquid viscosity for large MNPs. This means that , in a system with low viscosity such as water, the Brownian heating mechanism is significant due to the friction between the rotating MNPs and the surrounding medium.

https://doi.org/10.1021/acsomega.2c05962
ACS Omega 2023, 8, 12955−12967

It is important to mention that heat production mechanisms change depend on the size of MNPs as shown in Figure 5. For MNPs with SPM behavior, Néel relaxation dominates due to internal friction between the crystal lattice and the rotating magnetization. On increasing the size from the SPM to the ferromagnetic (FM) SD size regime, Brownian relaxation comes into play due to the friction between the rotating nanoparticles and the surrounding medium. The MNPs rotate in the ferrofluid while their magnetic moments remain fixed relative to the crystal orientation. For even larger MNPs, hysteresis losses are additionally contributing to the heating. Whenever a hysteresis loop is concluded, its area, corresponding to energy, is converted to heat. First, to explain the Néel or Brownian heating mechanism from the SPM to the SD region, magnetic hyperthermia measurements were taken (375 kHz/50 mT) for particle sizes from 16 to 37 nm, varying the viscosity of the medium using different agarose concentration from 2.5 to 30 mg mL^{-1} to restrict the MNP mobility in the medium (Figure 7a). In all cases, the concentration of MNPs was kept constant at 4 mg mL^{-1}. As can be seen in Figure 7a, the SLP values remain stable in small MNPs (16 nm), indicating that the heating mechanism is independent of the viscosity of the medium. This behavior indicates that the Néel relaxation mechanism is the dominant heating mechanism. For larger MNP diameters, the SLP values decrease with respect to the agarose concentration. This is due to the decreasing mobility of the MNPs in the medium, i.e. Brownian relaxation due to the physical rotation of the particles becoming more difficult.[85] However, the SLP values are constant above an agarose concentration of 20 mg mL^{-1} likely because the Brownian pathway is blocked, and another heating mechanism is dominant. Thus, heat generation via physical rotation is important at low viscosities and contributes about 50% to the SLP value.

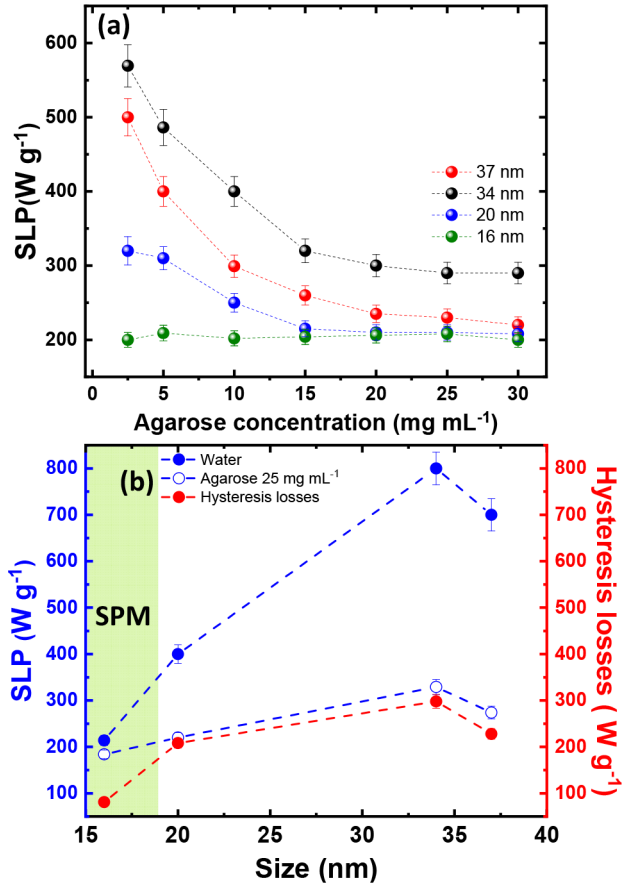

Figure 7. (a) SLP values as a function of agarose concentration varying from 2.5 to 30 mg mL^{-1} for diameters between 16 and 37 nm. (b) SLP values in two different media (water/agarose) at an MNP concentration of 4 mg mL^{-1} (50 mT/375 kHz) and hysteresis losses at a DC applied field of 50 mT (red dots) versus different MNP sizes from 16 to 37 nm.

From the above analysis, the question arises as to which is the dominant heating mechanism at higher agarose concentrations. Figure 7b summarizes the hysteresis losses at 50 mT and the SLP values in water and agarose (25 mg mL^{-1}) at at MNP concentration of 4 mg mL^{-1} (50 mT/375 kHz). By a direct comparison of hysteresis losses with magnetic hyperthermia measurements in water/agarose solution, the resemblance is unambiguous. Starting from MNPs with size of 16 nm, the values from hysteresis losses are basically zero due to the SPM behavior. However, the SLP values are higher than the magnetic losses and they have similar values in water and agarose. In this case, the Néel relaxation mechanism dominates due to internal friction between the crystal lattice and the rotating magnetization. Thus, the heat generation is independent of the medium viscosity. Further, with increasing size, a drastic decrease of SLP values was shown for MNP sizes from 20 to 37 nm oncomparing water and agarose media of different viscosities. It is observed that, by embedding the MNPs into high agarose concentration (>15 mg mL^{-1}), SLP values are found to be similar to the values of hysteresis losses. As a result, we expect to suppress or at least strongly reduce the Brownian losses due to the absence of the particle movement during MPH measurements. These results clearly reveal that the best strategy to enhance the heating efficiency, with respect to MNP size, is to increase the frequency and the AC field. Moreover, the heating rate of MNPs was improved by tuning their concentration. When the MNP size increases from the SPM to SD region, the heating mechanisms change, resulting in tunable heating efficiencies. However, we must note that the viscosity of the medium plays a crucial role in which heating mechanism is dominant. It was observed that SD particles have better heating efficiency than the SPM particles on decreasing the viscosity of the medium due to the Brown mechanism.

3.4. Low-Field Magnetic Particle Hyperthermia Measurements for Clinical Applications. The challenge for clinical applications is to tune the features of MNPs or to tune the applied magnetic field/frequency to achieve the hyperthermia limit 41−45 °C and to avoid overheating of healthy tissues. In the biological microenvironment, however, the MNPs can be immobilized in cells and as a result decrease their heating efficiency due to the Brown mechanism.[34,86,87] Thus, it is important to examine immobilized MNPs under hyperthermia measurements to find the optimum conditions for safe biological treatments. Additionally, for clinical trials there is a threshold where the maximum value of the product amplitude field × frequency should be less than 5×10^9 A m^{-1} s^{-1} to avoid neuromuscular electrostimulation and heat by eddy currents.[88−90]

According to the biological safety criteria, hyperthermia measurements were taken using a frequency of 103.6 kHz and applied magnetic fields varying from 20 to 40 mT. The biological microenvironment significantly influences the magnetic response of nanoparticles and can suppress Brownian

https://doi.org/10.1021/acsomega.2c05962
ACS Omega 2023, 8, 12955−12967

relaxation.[91] Thus, an agarose gel solution was used at a concentration of 2.5 mg mL^{-1} because it mimics the microstructure of soft tissues[92] and immobilizes the MNPs into the agarose matrix, while the concentration of MNPs was kept constant at 4 mg mL^{-1}. In these experiments, the product $H \times f$ ranges from 1.6×10^9 to 3.3×10^9 A m^{-1} s^{-1} for applied magnetic fields ranging from 20 to 40 mT and a frequency of 103.6 kHz. Starting from the highest fields (40 and 30 mT), all of the samples reached the hyperthermia limit 41−45 °C, while the AC field was applied for 480 s (Figure 8a and Figure S4a).

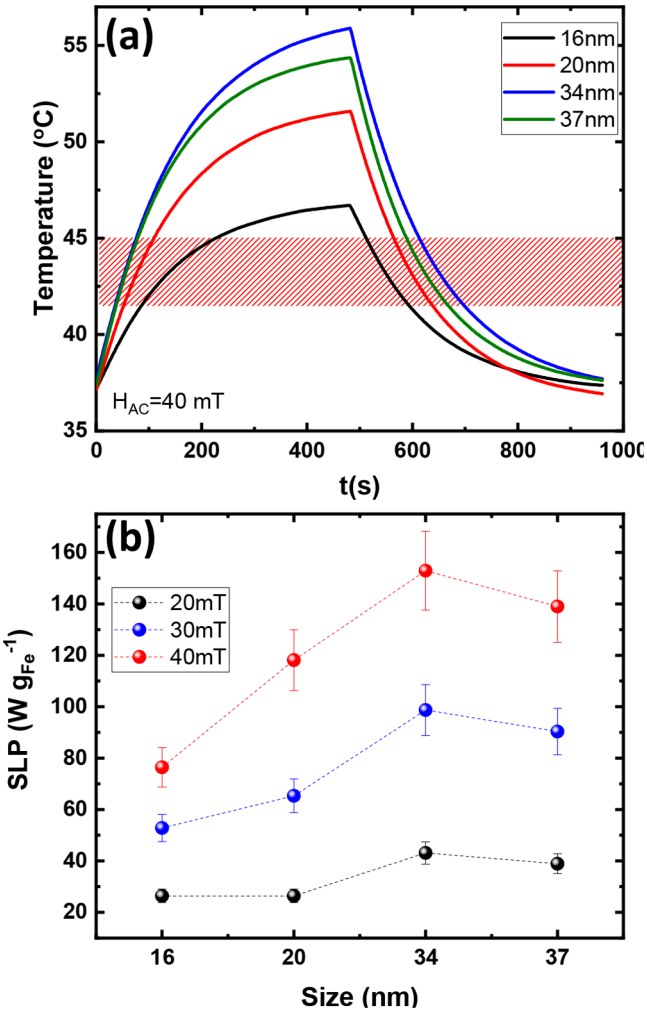

Figure 8. (a) Inductive heating curves of differently sized MNPs at 103.6 kHz and a concentration of 4 mg mL^{-1} at various sizes from 16 to 37 nm and an applied magnetic field of 40 mT. (b) SLP values under a low-field condition as a function of MNP size using three different applied magnetic fields from 20 to 40 mT at a low frequency of 103.6 kHz.

By decreasing the field to 20 mT (Figure S4b), only the samples with sizes of 34 and 37 nm overcome the hyperthermia region. That means, in a real clinical scenario MNPs with sizes from 16 to 37 nm could be used for hyperthermia treatment using magnetic fields of 30 and 40 mT. The SLP values under low-field conditions as a function of size are shown in Figure 8b. SLP values increased when the applied magnetic field was increased from 20 to 40 mT in all cases of samples, as shown in Figure 8b in black and red, respectively. However, the lowest increase of SLP values was observed for an applied field of 20 mT for all samples. The above results, for immobilized MNPs in agarose solution, present that the MNPs from 16 to 37 nm can be used in hyperthermia treatment in a real clinical scenario when the magnetic field is greater than 20 mT to reach the therapeutic window of 41−45 °C.

4. CONCLUSIONS

In summary, magnetite MNPs were prepared by a coprecipitation method, which is an eco-friendly approach with facile synthetic control. XRD patterns and TEM/HRTEM images established that MNPs are single-crystalline magnetite nanoparticles of various sizes. The size of MNPs was adjusted from 16 to 76 nm by setting the pH values of the solutions from 9.0 to 13.5. The magnetic responses of MNPs were evaluated with respect to their size. Magnetic measurements reveal that smallest MNPs are superparamagnetic, the medium sizes are single-domain ferromagnets, and the largest MNPs are at the transition to a multidomain. Magnetic hyperthermia measurements were conducted as a function of sample features (concentration, medium) and field conditions (amplitude, frequency). First, the dosage of MNPs was examined by varying the concentration from 1 to 4 mg mL^{-1}. Hyperthermia measurements have shown that the effective heating, as expressed by SLP values, tends to increase with MNP concentration in all cases of particle size. When the MNP concentration is increased, the interparticle distances decrease and thereby the dipolar interactions are enhanced, leading to increasing SLP values. The best heating results have been obtained in the ferromagnetic, single-domain region. More specifically, the maximum SLP values were obtained for a concentration of 4 mg mL^{-1} (1450 and 1050 W g^{-1} for 34 and 37 nm at 765 kHz/30 mT, respectively). Afterward, the AC field hyperthermia conditions were examined for two frequencies (375 and 765 kHz) and AC fields ranging from 20 to 50 mT. The hyperthermia measurements reveal that the heating efficiency increases as a function of frequency. Analogously, the AC field amplitude also promotes higher SLP values by increasing the size from SPM to FM. The heating efficiency is proportional to the square of the applied field (H^2) for MNPs sizes from 16 to 37 nm. Importantly, the fitted factor of the H^2 dependence has been related to the magnetic profile of the MNPs and the viscosity of the medium, confirming different heating mechanisms. To analyze the mechanisms of heating, MNPs were measured in water and agarose using identical hyperthermia conditions (375 kHz/50 mT). Moreover, hysteresis losses for minor loops from 20 to 50 mT were compared with the hyperthermia losses. The experimental results show that, in the SPM regime, the heat generation is mainly due to Néel relaxation. In contrast, Brownian and hysteresis losses dominate for particle sizes from 20 to 37 nm with ferromagnetic behavior at room temperature. Most importantly, we have shown that Brownian and hysteresis losses contribute equally to the heating in this size regime at low viscosities. With increasing medium (tissue) viscosity, however, Brownian losses gradually decrease while hysteresis losses remain as the dominant heating source in stiff media. The above results confirm that the concentration of MNPs and the frequency and amplitude of the applied field should be handled differently with respect to MNP size and eventually to their collective magnetic features, to promote efficient heat delivery in magnetic hyperthermia schemes. Finally, the heating efficiency of immobilized MNPs in agarose solution under low-field conditions (30−40 mT/103 kHz)

https://doi.org/10.1021/acsomega.2c05962
ACS Omega 2023, 8, 12955−12967

using different sizes from 16 to 37 nm meets the requirements of hyperthermia treatment for clinical application to avoid neuromuscular electrostimulation and heat by eddy currents.

■ ASSOCIATED CONTENT

Supporting Information

The Supporting Information is available free of charge at https://pubs.acs.org/doi/10.1021/acsomega.2c05962.

Size distribution of the magnetite MNPs with different pH values from 9.0 to 13.5, hyperthermia curves for MNPs with sizes from 16 to 76 nm for an applied field of 30 mT and frequency of 765 kHz on varying the MNP concentration from 1 to 4 mg mL^{-1}, hyperthermia curves with a concentration of 4 mg mL^{-1} at different applied magnetic fields from 20 to 50 mT using a frequency of 375 kHz for MNP sizes from 16 to 37 nm, and inductive heating curves of differently sized MNPs at 103 kHz and a concentration of 4 mg mL^{-1} at various sizes from 16 to 76 nm and different applied magnetic fields (PDF)

■ AUTHOR INFORMATION

Corresponding Author

Ulf Wiedwald − *Faculty of Physics and Center for Nanointegration Duisburg-Essen (CENIDE), University of Duisburg-Essen, Duisburg 47048, Germany;* orcid.org/0000-0002-3209-4078; Phone: +49 203 3792633; Email: ulf.wiedwald@uni-due.de

Authors

Eirini Myrovali − *School of Physics, Aristotle University of Thessaloniki, Thessaloniki 54124, Greece; MagnaCharta, Center for Interdisciplinary Research and Innovation (CIRI-AUTH), Thessaloniki 57001, Greece;* orcid.org/0000-0003-0193-3470

Kyrillos Papadopoulos − *School of Physics, Aristotle University of Thessaloniki, Thessaloniki 54124, Greece; MagnaCharta, Center for Interdisciplinary Research and Innovation (CIRI-AUTH), Thessaloniki 57001, Greece*

Georgia Charalampous − *School of Physics, Aristotle University of Thessaloniki, Thessaloniki 54124, Greece*

Paraskevi Kesapidou − *School of Physics, Aristotle University of Thessaloniki, Thessaloniki 54124, Greece*

George Vourlias − *School of Physics, Aristotle University of Thessaloniki, Thessaloniki 54124, Greece*

Thomas Kehagias − *School of Physics, Aristotle University of Thessaloniki, Thessaloniki 54124, Greece*

Makis Angelakeris − *School of Physics, Aristotle University of Thessaloniki, Thessaloniki 54124, Greece; MagnaCharta, Center for Interdisciplinary Research and Innovation (CIRI-AUTH), Thessaloniki 57001, Greece;* orcid.org/0000-0001-9109-0221

Complete contact information is available at: https://pubs.acs.org/10.1021/acsomega.2c05962

Notes

The authors declare no competing financial interest.

■ ACKNOWLEDGMENTS

This work was supported by the European Union's Horizon 2020 research and innovation program under grant agreement No. 857502 (MaNaCa).

■ REFERENCES

(1) Kefeni, K. K.; Msagati, T. A.; Mamba, B. Ferrite nanoparticles: synthesis, characterisation and applications in electronic device. *Mater. Sci. Eng. B* **2017**, *215*, 37−55.

(2) Weissig, V.; Pettinger, T. K.; Murdock, N. Nanopharmaceuticals (part 1): products on the market. *Int. J. Nanomedicine.* **2014**, *9*, 4357.

(3) Zhu, L.; Zhou, Z.; Mao, H.; Yang, L. Magnetic nanoparticles for precision oncology: theranostic magnetic iron oxide nanoparticles for image-guided and targeted cancer therapy. *Nanomed. J.* **2017**, *12* (1), 73−87.

(4) Gao, M. R.; Zhang, S. R.; Jiang, J.; Zheng, Y. R.; Tao, D. Q.; Yu, S. H. One-pot synthesis of hierarchical magnetite nanochain assemblies with complex building units and their application for water treatment. *J. Mater. Chem.* **2011**, *21* (42), 16888−16892.

(5) Myrovali, E. Hybrid Stents Based on Magnetic Hydrogels for Biomedical Applications. *ACS Appl. Bio Mater.* **2022**, *5*, 2598.

(6) Al-Anazi, A. Iron-based magnetic nanomaterials in environmental and energy applications: a short review. *Curr. Opin. Chem.* **2022**, *36*, 100794.

(7) Wu, W.; Jiang, C. Z.; Roy, V. A. Designed synthesis and surface engineering strategies of magnetic iron oxide nanoparticles for biomedical applications. *Nanoscale* **2016**, *8* (47), 19421−19474.

(8) Albarqi, H. A.; Wong, L. H.; Schumann, C.; Sabei, F. Y.; Korzun, T.; Li, X.; Hansen, M. N.; Dhagat, P.; Moses, A. S.; Taratula, O.; Taratula, O. Biocompatible nanoclusters with high heating efficiency for systemically delivered magnetic hyperthermia. *ACS Nano* **2019**, *13* (6), 6383−6395.

(9) Grauer, O.; Jaber, M.; Hess, K.; Weckesser, M.; Schwindt, W.; Maring, S.; Wölfer, J.; Stummer, W. Combined intracavitary thermotherapy with iron oxide nanoparticles and radiotherapy as local treatment modality in recurrent glioblastoma patients. *J. Neuro-Oncol.* **2019**, *141* (1), 83−94.

(10) Maier-Hauff, K.; Ulrich, F.; Nestler, D.; Niehoff, H.; Wust, P.; Thiesen, B.; Orawa, H.; Budach, V.; Jordan, A. Efficiency and safety of intratumoral thermotherapy using magnetic iron-oxide nanoparticles combined with external beam radiotherapy on patients with recurrent glioblastoma multiforme. *J. Neuro-Oncol.* **2011**, *103* (2), 317−324.

(11) Thiesen, B.; Jordan, A. Clinical applications of magnetic nanoparticles for hyperthermia. *Int. J. Hyperth.* **2008**, *24* (6), 467−474.

(12) Johannsen, M.; Gneveckow, U.; Eckelt, L.; Feussner, A.; Waldöfner, N.; Scholz, R.; Deger, S.; Wust, P.; Loening, S. A.; Jordan, A. Clinical hyperthermia of prostate cancer using magnetic nanoparticles: presentation of a new interstitial technique. *Int. J. Hyperth.* **2005**, *21* (7), 637−647.

(13) Johannsen, M.; Gneveckow, U.; Thiesen, B.; Taymoorian, K.; Cho, C. H.; Waldöfner, N.; Scholz, R.; Jordan, A.; Loening, S. A.; Wust, P. Thermotherapy of prostate cancer using magnetic nanoparticles: feasibility, imaging, and threedimensional temperature distribution. *Eur. Urol* **2007**, *52* (6), 1653−1661.

(14) Sampora, Y.; Hardiansyah, A.; Khaerudini, D. S.; Burhani, D.; Sondari, D.; Septiyanti, M.; Septevani, A. Synthesis and characterization of magnetite nanoparticle for removal of heavy metal ions from aqueous solutions. *IOP Conf. Ser. Earth Environ. Sci.* **2022**, *1017* (1), 012017.

(15) Naz, M. Y.; Shukrullah, S.; Ghaffar, A.; Ali, K.; Sharma, S. K. In *Synthesis and processing of nanomaterials in Solar Cells, From Materials to Device Technology*; Sharma, S. K., Khuram, A., Eds.; Springer: 2020; *1*−*23*.

(16) Kolluru, S. S.; Agarwal, S.; Sireesha, S.; Sreedhar, I.; Kale, S. R. Heavy metal removal from wastewater using nanomaterials-process and engineering aspects. *Process Saf. Environ. Prot.* **2021**, *150*, 323−355.

(17) Yusoff, A. H.; Salimi, M. N.; Jamlos, M. F. A review: Synthetic strategy control of magnetite nanoparticles production. *Adv. Nano Res.* **2018**, *6* (1), 1.

(18) Luengo, Y.; Morales, M. D. P.; Gutiérrez, L.; Veintemillas-Verdaguer, S. Counterion and solvent effects on the size of magnetite

nanocrystals obtained by oxidative precipitation. *J. Mater. Chem. C* **2016**, *4* (40), 9482−9488.
(19) Koizumi, H.; Uddin, M. A.; Kato, Y. Effect of ultrasonic irradiation on γ-Fe_2O_3 formation by co-precipitation method with Fe^{3+} salt and alkaline solution. *Inorg. Chem. Commun.* **2021**, *124*, 108400.
(20) Andres Verges, M; Costo, R; Roca, A G; Marco, J F; Goya, G F; Serna, C J; Morales, M P Uniform and water stable magnetite nanoparticles with diameters around the monodomain-multidomain limit. *J. Phys. D: Appl. Phys.* **2008**, *41* (13), 134003.
(21) Hergt, R.; Dutz, S.; Müller, R.; Zeisberger, M. Magnetic particle hyperthermia: nanoparticle magnetism and materials development for cancer therapy. *J. Condens. Matter Phys.* **2006**, *18* (38), S2919.
(22) Gavilán, H.; Simeonidis, K.; Myrovali, E.; Mazarío, E.; Chubykalo-Fesenko, O.; Chantrell, R.; Balcells, Ll.; Angelakeris, M.; Morales, M. P.; Serantes, D. How size, shape and assembly of magnetic nanoparticles give rise to different hyperthermia scenarios. *Nanoscale* **2021**, *13* (37), 15631−15646.
(23) Baker, I.; Zeng, Q.; Li, W.; Sullivan, C. R. Heat deposition in iron oxide and iron nanoparticles for localized hyperthermia. *J. Appl. Phys.* **2006**, *99* (8), 08H106.
(24) Tong, S.; Quinto, C. A.; Zhang, L.; Mohindra, P.; Bao, G. Size-dependent heating of magnetic iron oxide nanoparticles. *ACS Nano* **2017**, *11* (7), 6808−6816.
(25) Angelakeris, M. Magnetic nanoparticles: A multifunctional vehicle for modern theranostics. *Biochim. Biophys. Acta Gen. Subj.* **2017**, *1861* (6), 1642−1651.
(26) Rosensweig, R. E. Heating magnetic fluid with alternating magnetic field. *J. Magn. Magn. Mater.* **2002**, *252*, 370−374.
(27) Dennis, C. L.; Ivkov, R. Physics of heat generation using magnetic nanoparticles for hyperthermia. *Int. J. Hyperth.* **2013**, *29* (8), 715−729.
(28) Kandasamy, G.; Sudame, A.; Bhati, P.; Chakrabarty, A.; Maity, D. Systematic investigations on heating effects of carboxyl-amine functionalized superparamagnetic iron oxide nanoparticles (SPIONs) based ferrofluids for in vitro cancer hyperthermia therapy. *J. Mol. Liq.* **2018**, *256*, 224−237.
(29) Wan, J.; Yuan, R.; Zhang, C.; Wu, N.; Yan, F.; Yu, S.; Chen, K. Stable and biocompatible colloidal dispersions of superparamagnetic iron oxide nanoparticles with minimum aggregation for biomedical applications. *J. Phys. Chem. C* **2016**, *120* (41), 23799−23806.
(30) Mehdaoui, B.; Tan, R. P.; Meffre, A.; Carrey, J.; Lachaize, S.; Chaudret, B.; Respaud, M. Increase of magnetic hyperthermia efficiency due to dipolar interactions in low-anisotropy magnetic nanoparticles: Theoretical and experimental results. *Phys. Rev. B* **2013**, *87* (17), 174419.
(31) Zufelato, N.; Aquino, V. R.; Shrivastava, N.; Mendanha, S.; Miotto, R.; Bakuzis, A. F. Heat Generation in Magnetic Hyperthermia by Manganese Ferrite-Based Nanoparticles Arises from Néel Collective Magnetic Relaxation. *ACS Appl. Nano Mater.* **2022**, *5*, 7521−7539.
(32) Blanco-Andujar, C.; Ortega, D.; Southern, P.; Nesbitt, S. A.; Thanh, N. T. K.; Pankhurst, Q. A. Real-time tracking of delayed-onset cellular apoptosis induced by intracellular magnetic hyperthermia. *Nanomedicine* **2016**, *11* (2), 121−136.
(33) Efremova, M. V.; Nalench, Y. A.; Myrovali, E.; Garanina, A. S.; Grebennikov, I. S.; Gifer, P. K.; Abakumov, M. A.; Spasova, M.; Angelakeris, M.; Savchenko, A. G.; Farle, M.; Klyachko, N. L.; Majouga, A. G.; Wiedwald, U. Size-selected Fe_3O_4-Au hybrid nanoparticles for improved magnetism-based theranostics. *Beilstein J. Nanotechnol.* **2018**, *9* (1), 2684−2699.
(34) Di Corato, R.; Espinosa, A.; Lartigue, L.; Tharaud, M.; Chat, S.; Pellegrino, T.; Ménager, C.; Gazeau, F.; Wilhelm, C. Magnetic hyperthermia efficiency in the cellular environment for different nanoparticle designs. *Biomaterials* **2014**, *35* (24), 6400−6411.
(35) Myrovali, E.; Maniotis, N.; Makridis, A.; Terzopoulou, A.; Ntomprougkidis, V.; Simeonidis, K.; Sakellari, D.; Kalogirou, O.; Samaras, T.; Salikhov, R.; Spasova, M.; Farle, M.; Wiedwald, U.; Angelakeris, M. Arrangement at the nanoscale: Effect on magnetic particle hyperthermia. *Sci. Rep.* **2016**, *6* (1), 1−11.
(36) Soukup, D.; Moise, S.; Céspedes, E.; Dobson, J.; Telling, N. D. In situ measurement of magnetization relaxation of internalized nanoparticles in live cells. *ACS Nano* **2015**, *9* (1), 231−240.
(37) Cabrera, D.; Camarero, J.; Ortega, D.; Teran, F. J. Influence of the aggregation, concentration, and viscosity on the nanomagnetism of iron oxide nanoparticle colloids for magnetic hyperthermia. *J. Nanoparticle Res.* **2015**, *17* (3), 1−6.
(38) Guardia, P.; Di Corato, R.; Lartigue, L.; Wilhelm, C.; Espinosa, A.; Garcia-Hernandez, M.; Gazeau, F.; Manna, L.; Pellegrino, T. Water-soluble iron oxide nanocubes with high values of specific absorption rate for cancer cell hyperthermia treatment. *ACS Nano* **2012**, *6* (4), 3080−3091.
(39) Fortin, J. P.; Wilhelm, C.; Servais, J.; Ménager, C.; Bacri, J. C.; Gazeau, F. Size-sorted anionic iron oxide nanomagnets as colloidal mediators for magnetic hyperthermia. *J. Am. Chem. Soc.* **2007**, *129* (9), 2628−2635.
(40) Myrovali, E.; Maniotis, N.; Samaras, T.; Angelakeris, M. Spatial focusing of magnetic particle hyperthermia. *Nanoscale Adv.* **2020**, *2* (1), 408−416.
(41) Shah, R. R.; Davis, T. P.; Glover, A. L.; Nikles, D. E.; Brazel, C. S. Impact of magnetic field parameters and iron oxide nanoparticle properties on heat generation for use in magnetic hyperthermia. *J. Magn. Magn. Mater.* **2015**, *387*, 96−106.
(42) Myrovali, E.; Papadopoulos, K.; Iglesias, I.; Spasova, M.; Farle, M.; Wiedwald, U.; Angelakeris, M. Long-Range Ordering Effects in Magnetic Nanoparticles. *ACS Appl. Mater. Interfaces.* **2021**, *13* (18), 21602−21612.
(43) Chalkidou, A.; Simeonidis, K.; Angelakeris, M.; Samaras, T.; Martinez-Boubeta, C.; Balcells, Ll.; Papazisis, K.; Dendrinou-Samara, C.; Kalogirou, O. In Vitro Application of Fe/MgO Nanoparticles as Magnetically Mediated Hyperthermia Agents for Cancer Treatment. *J. Magn. Magn. Mater.* **2011**, *323*, 775−780.
(44) Al Mamun, A.; Onoguchi, A.; Granata, G.; Tokoro, C. Role of pH in green rust preparation and chromate removal from water. *Appl. Clay Sci.* **2018**, *165*, 205−213.
(45) Granath, T.; Löbmann, P.; Mandel, K. Oxidative Precipitation as a Versatile Method to Obtain Ferromagnetic Fe_3O_4 Nano-and Mesocrystals Adjustable in Morphology and Magnetic Properties. *Part. Part. Syst. Charact.* **2021**, *38* (3), 2000307.
(46) Russell, M. J. Green rust: the simple organizing 'seed'of all life? *Life* **2018**, *8* (3), 35.
(47) Navarro, E.; Luengo, Y.; Veintemillas, S.; Morales, P.; Palomares, F. J.; Urdiroz, U.; Cebollada, F.; González, J. M. Temperature dependence of the magnetic interactions taking place in monodisperse magnetite nanoparticles having different morphologies. *AIP Adv.* **2021**, *11* (1), 015025.
(48) Roca, A. G.; Gutiérrez, L.; Gavilán, H.; Brollo, M. E. F.; Veintemillas-Verdaguer, S.; del Puerto Morales, M. Design strategies for shape-controlled magnetic iron oxide nanoparticles. *Adv. Drug Delivery Rev.* **2019**, *138*, 68−104.
(49) Cullity, B. D. *Introduction to Magnetic Materials*; Addison-Wesley: 1972.
(50) Andrzejewski, B.; Bednarski, W.; Kaźmierczak, M.; Łapiński, A.; Pogorzelec-Glaser, K.; Hilczer, B.; Jurga, S.; Nowaczyk, G.; Załęski, K.; Matczaka, M.; Łęskac, B.; Pankiewicz, R.; Kępińskid, L. Magnetization enhancement in magnetite nanoparticles capped with alginic acid. *Compos. B. Eng.* **2014**, *64*, 147−154.
(51) Kostopoulou, A.; Brintakis, K.; Vasilakaki, M.; Trohidou, K. N.; Douvalis, A. P.; Lascialfari, A.; Manna, L.; Lappas, A. Assembly-mediated interplay of dipolar interactions and surface spin disorder in colloidal maghemite nanoclusters. *Nanoscale* **2014**, *6* (7), 3764−3776.
(52) Coey, J. M. D. Noncollinear spin arrangement in ultrafine ferrimagnetic crystallites. *Phys. Rev. Lett.* **1971**, *27* (17), 1140.
(53) Fiorani, D.; Testa, A. M.; Lucari, F.; D'orazio, F.; Romero, H. Magnetic properties of maghemite nanoparticle systems: surface anisotropy and interparticle interaction effects. *Phys. B: Condens. Matter* **2002**, *320* (1−4), 122−126.

https://doi.org/10.1021/acsomega.2c05962
ACS Omega 2023, 8, 12955−12967

(54) Goya, G. F.; Berquo, T. S.; Fonseca, F. C.; Morales, M. P. Static and dynamic magnetic properties of spherical magnetite nanoparticles. *J. Appl. Phys.* **2003**, *94* (5), 3520−3528.
(55) Woińska, M.; Szczytko, J.; Majhofer, A.; Gosk, J.; Dziatkowski, K.; Twardowski, A. Magnetic interactions in an ensemble of cubic nanoparticles: A Monte Carlo study. *Phys. Rev. B* **2013**, *88* (14), 144421.
(56) Guzdial, M. From science to engineering. *Commun. ACM* **2011**, *54* (2), 37−39.
(57) Hergt, R.; Dutz, S.; Röder, M. Effects of size distribution on hysteresis losses of magnetic nanoparticles for hyperthermia. *J. Condens. Matter Phys.* **2008**, *20* (38), 385214.
(58) Li, Q.; Kartikowati, C. W.; Horie, S.; Ogi, T.; Iwaki, T.; Okuyama, K. Correlation between particle size/domain structure and magnetic properties of highly crystalline Fe_3O_4 nanoparticles. *Sci. Rep.* **2017**, *7* (1), 1−7.
(59) Eagle, D. F.; Mallinson, J. C. On the coercivity of γ-Fe_2O_3 particles. *J. Appl. Phys.* **1967**, *38*, 995−997.
(60) Colombo, M.; Carregal-Romero, S.; Casula, M. F.; Gutiérrez, L.; Morales, M. P.; Böhm, I. B.; Heverhagen, J. T.; Prosperi, D.; Parak, W. J. Biological applications of magnetic nanoparticles. *Chem. Soc. Rev.* **2012**, *41* (11), 4306−4334.
(61) Heider, F.; Dunlop, D. J.; Sugiura, N. Magnetic properties of hydrothermally recrystallized magnetite crystals. *Science* **1987**, *236* (4806), 1287−1290.
(62) Dutz, S.; Hergt, R.; Mürbe, J.; Müller, R.; Zeisberger, M.; Andrä, W.; Töpfer, J.; Bellemann, M. E. Hysteresis losses of magnetic nanoparticle powders in the single domain size range. *J. Magn. Magn. Mater.* **2007**, *308* (2), 305−312.
(63) Pawlik, P.; Blasiak, B.; Depciuch, J.; Pruba, M.; Kitala, D.; Vorobyova, S.; Stec, M.; Bushinsky, M.; Konakov, A.; Baran, J.; Fedotova, J.; Ivashkevich, O.; Parlinska-Wojtan, M.; Maximenko, A. Application of iron-based magnetic nanoparticles stabilized with triethanolammonium oleate for theranostics. *J. Mater. Sci.* **2022**, *57* (7), 4716−4737.
(64) Piñeiro-Redondo, Y.; Bañobre-López, M.; Pardiñas-Blanco, I.; Goya, G.; López-Quintela, M. A.; Rivas, J. The influence of colloidal parameters on the specific power absorption of PAA-coated magnetite nanoparticles. *Nanoscale Res. Lett.* **2011**, *6* (1), 1−7.
(65) Kim, J. W.; Wang, J.; Kim, H.; Bae, S. Concentration-dependent oscillation of specific loss power in magnetic nanofluid hyperthermia. *Sci. Rep.* **2021**, *11* (1), 1−10.
(66) Deatsch, A. E.; Evans, B. A. Heating efficiency in magnetic nanoparticle hyperthermia. *J. Magn. Magn. Mater.* **2014**, *354*, 163−172.
(67) Salas, G.; Camarero, J.; Cabrera, D.; Takacs, H.; Varela, M.; Ludwig, R.; Dähring, H.; Hilger, I.; Miranda, R.; del Puerto Morales, M.; Teran, F. J. Modulation of magnetic heating via dipolar magnetic interactions in monodisperse and crystalline iron oxide nanoparticles. *J. Phys. Chem. C* **2014**, *118* (34), 19985−19994.
(68) Landi, G. T. Role of dipolar interaction in magnetic hyperthermia. *Phys. Rev. B* **2014**, *89* (1), 014403.
(69) De la Presa, P.; Luengo, Y.; Multigner, M.; Costo, R.; Morales, M. P.; Rivero, G.; Hernando, A. Study of heating efficiency as a function of concentration, size, and applied field in γ-Fe_2O_3 nanoparticles. *J. Phys. Chem. C* **2012**, *116* (48), 25602−25610.
(70) Serantes, D.; Simeonidis, K.; Angelakeris, M.; Chubykalo-Fesenko, O.; Marciello, M.; Morales, M. d. P.; Baldomir, D.; Martinez-Boubeta, C. Multiplying magnetic hyperthermia response by nanoparticle assembling. *J. Phys. Chem. C* **2014**, *118* (11), 5927−5934.
(71) Serantes, D.; Baldomir, D.; Martinez-Boubeta, C.; Simeonidis, K.; Angelakeris, M.; Natividad, E.; Castro, M.; Mediano, A.; Chen, D.-X.; Sanchez, A.; Balcells, L. I.; Martínez, B. Influence of dipolar interactions on hyperthermia properties of ferromagnetic particles. *J. Appl. Phys.* **2010**, *108* (7), 073918.
(72) Dutz, S.; Hergt, R. Magnetic nanoparticle heating and heat transfer on a microscale: Basic principles, realities and physical limitations of hyperthermia for tumour therapy. *Int. J. Hyperth.* **2013**, *29* (8), 790−800.
(73) Dutz, S.; Hergt, R. Magnetic particle hyperthermia—a promising tumour therapy. *Nanotechnology* **2014**, *25* (45), 452001.
(74) Bertotti, G. *Hysteresis in magnetism: for physicists, materials scientists, and engineers*; Gulf Professional Publishing: 1998.
(75) Carrey, J.; Boubker, M.; Marc, R. Simple models for dynamic hysteresis loop calculations of magnetic single-domain nanoparticles: Application to magnetic hyperthermia optimization. *J. Appl. Phys.* **2011**, *109* (8), 083921.
(76) Martinez-Boubeta, C.; Simeonidis, K.; Serantes, D.; Conde-Leborán, I.; Kazakis, I.; Stefanou, G.; Peña, L.; Galceran, R.; Balcells, L.; Monty, C.; Baldomir, D.; Mitrakas, M.; Angelakeris, M. Adjustable hyperthermia response of self-assembled ferromagnetic Fe-MgO core-shell nanoparticles by tuning dipole-dipole interactions. *Adv. Funct. Mater.* **2012**, *22* (17), 3737−3744.
(77) Carrey, J.; Mehdaoui, B.; Respaud, M. Magnetic memory effect of nanocomposites. *J. Appl, Phys.* **2011**, *109*, 083921.
(78) Usov, N. A.; Liubimov, B. Y. Dynamics of magnetic nanoparticle in a viscous liquid: Application to magnetic nanoparticle hyperthermia. *J. Appl. Phys.* **2012**, *112* (2), 023901.
(79) Simeonidis, K.; Martinez-Boubeta, C.; Balcells, L.; Monty, C.; Stavropoulos, G.; Mitrakas, M.; Matsakidou, A.; Vourlias, G.; Angelakeris, M. Fe-based nanoparticles as tunable magnetic particle hyperthermia agents. *J. Appl. Phys.* **2013**, *114* (10), 103904.
(80) Soetaert, F.; Kandala, S. K.; Bakuzis, A.; Ivkov, R. Experimental estimation and analysis of variance of the measured loss power of magnetic nanoparticles. *Sci. Rep.* **2017**, *7* (1), 1−15.
(81) Torres, T. E.; Lima, E.; Calatayud, M. P.; Sanz, B.; Ibarra, A.; Fernández-Pacheco, R.; Mayoral, A.; Marquina, C.; Ibarra, M. R.; Goya, G. F. The relevance of Brownian relaxation as power absorption mechanism in Magnetic Hyperthermia. *Sci. Rep.* **2019**, *9* (1), 1−11.
(82) Usov, N. A. R. A.; Rytov, V.; Bautin, A. Properties of assembly of superparamagnetic nanoparticles in viscous liquid. *Sci. Rep.* **2021**, *11* (1), 1−11.
(83) Salas, G.; Veintemillas-Verdaguer, S.; Morales, M. D. P. Relationship between physico-chemical properties of magnetic fluids and their heating capacity. *Int. J. Hyperth.* **2013**, *29* (8), 768−776.
(84) Carrey, J.; Mehdaoui, B.; Respaud, M. Simple models for dynamic hysteresis loop calculations of magnetic single-domain nanoparticles: Application to magnetic hyperthermia optimization. *Int. J. Appl. Phys.* **2011**, *109* (8), 083921.
(85) Morales, I.; Costo, R.; Mille, N.; Carrey, J.; Hernando, A.; de la Presa, P. Time-dependent AC magnetometry and chain formation in magnetite: the influence of particle size, initial temperature and the shortening of the relaxation time by the applied field. *Nanoscale Adv.* **2021**, *3* (20), 5801−5812.
(86) Dutz, S.; Kettering, M.; Hilger, I.; Müller, R.; Zeisberger, M. Magnetic multicore nanoparticles for hyperthermia—influence of particle immobilization in tumour tissue on magnetic properties. *Nanotechnology* **2011**, *22* (26), 265102.
(87) Bender, P.; Fock, J.; Frandsen, C.; Hansen, M. F.; Balceris, C.; Ludwig, F.; Posth, O.; Wetterskog, E.; Bogart, L. K.; Southern, P.; Szczerba, W.; Zeng, L.; Witte, K.; Grüttner, C.; Westphal, F.; Honecker, D.; González-Alonso, D.; Barquín, L. F.; Johansson, C. Relating magnetic properties and high hyperthermia performance of iron oxide nanoflowers. *J. Phys. Chem. C* **2018**, *122* (5), 3068−3077.
(88) Atkinson, W. J.; Brezovich, I. A.; Chakraborty, D. P. Usable frequencies in hyperthermia with thermal seeds. *IEEE. Trans. Biomed. Eng.* **1984**, *BME-31* (1), 70−75.
(89) Mehdaoui, B.; Meffre, A.; Carrey, J.; Lachaize, S.; Lacroix, L. M.; Gougeon, M.; Chaudret, B.; Respaud, M. Optimal size of nanoparticles for magnetic hyperthermia: a combined theoretical and experimental study. *Adv. Funct. Mater.* **2011**, *21* (23), 4573−4581.
(90) Rodrigues, H. F.; Capistrano, G.; Bakuzis, A. F. In vivo magnetic nanoparticle hyperthermia: A review on preclinical studies, low-field nano-heaters, noninvasive thermometry and computer simulations for treatment planning. *Int. J. Hyperth.* **2020**, *37* (3), 76−99.

https://doi.org/10.1021/acsomega.2c05962
ACS Omega 2023, 8, 12955−12967

(91) Soukup, D.; Moise, S.; Céspedes, E.; Dobson, J.; Telling, N. D. In situ measurement of magnetization relaxation of internalized nanoparticles in live cells. *ACS Nano* **2015**, *9* (1), 231−240.
(92) Salloum, M.; Ma, R. H.; Weeks, D.; Zhu, L. Controlling nanoparticle delivery in magnetic nanoparticle hyperthermia for cancer treatment: experimental study in agarose gel. *Int. J. Hyperth.* **2008**, *24* (4), 337−345.

https://doi.org/10.1021/acsomega.2c05962
ACS Omega 2023, 8, 12955−12967